NEPSC2, the North Ecliptic Pole SCUBA-2 survey: 850-m map and catalogue of 850-m selected sources over 2 deg^2

Journal Item

NEPSC2, the North Ecliptic Pole SCUBA-2 survey: 850-μm map and catalogue of 850-μm selected sources over 2 deg^2

Hyunjin Shim,[1]★ Yeonsik Kim,[2] Dongseob Lee,[1] Hyung Mok Lee,[3,4] Tomo Goto,[5] Hideo Matsuhara,[6] Douglas Scott,[7] Stephen Serjeant,[8] Yiping Ao,[9,10] Laia Barrufet,[11,12] Scott Chapman,[13] David L. Clements,[14] Christopher J. Conselice,[15] Thomas R. Greve,[16,17,18] Tetsuya Hashimoto,[5,19] Ho Seong Hwang,[3] Myungshin Im,[4] Woong-Seob Jeong,[3] Linhua Jiang,[20] Minjin Kim,[2] Seong Jin Kim,[5] Albert K. H. Kong,[5] Maciej Koprowski,[21] Lucia Marchetti,[22,23,8] Michał J. Michałowski,[24] Harriet Parsons,[25] Chris Pearson,[8,12,26] Hyunjong Seo,[3] Yoshiki Toba,[27,28,29] and Glenn White[8]

[1] *Department of Earth Science Education, Kyungpook National University, Daegu 41566, Republic of Korea*
[2] *Department of Astronomy and Atmospheric Sciences, Kyungpook National University, Daegu 41566, Republic of Korea*
[3] *Korea Astronomy and Space Science Institute, Daejeon 34055, Republic of Korea*
[4] *Department of Physics and Astronomy, Seoul National University, Seoul 08826, Republic of Korea*
[5] *Institute of Astronomy, National Tsing Hua University, 101, Section 2. Kuang-Fu Road, Hsinchu, 30013, Taiwan (R.O.C.)*
[6] *Institute of Space and Astronautical Science, Japan Aerospace Exploration Agency, 3-1-1 Yoshinodai, Chuo, Sagamihara, Kanagawa 252-5210, Japan*
[7] *Department of Physics and Astronomy, University of British Columbia, Canada*
[8] *The Open University, Milton Keynes, MK7 6AA, UK*
[9] *Purple Mountain Observatory and Key Laboratory for Radio Astronomy, Chinese Academy of Sciences, Nanjing, China*
[10] *School of Astronomy and Space Science, University of Science and Technology of China, Hefei, Anhui, China*
[11] *European Space Astronomy Center, 28691 Villanueva de la Cañada, Spain*
[12] *RAL Space, STFC Rutherford Appleton Laboratory, Didcot, Oxfordshire OX11 0QX, UK*
[13] *Department of Physics and Atmospheric Science, Dalhouise University, Halifax, NS B3H 4R2, Canada*
[14] *Imperial College London, Blackett Lab., Prince Consort Road, London, SW7 2AZ, UK*
[15] *University of Nottingham, School of Physics & Astronomy, Nottingham NG7 2RD, UK*
[16] *Department of Physics and Astronomy, University College London, Gower Street, London WC1E 6BT, UK*
[17] *Cosmic Dawn Center*
[18] *National Space Institute, DTU Space, Technical University of Denmark, Elektrovej 327, DK-2800 Kgs. Lyngby, Denmark*
[19] *Centre for Informatics and Computation in Astronomy (CICA), National Tsing Hua University, 101, Section 2. Kuang-Fu Road, Hsinchu, 30013, Taiwan (R.O.C.)*
[20] *Kavli Institute for Astronomy and Astrophysics, Peking University, No.5 Yiheyuan Road, Haidian District, Beijing 100871, P. R. China*
[21] *Institute of Astronomy, Faculty of Physics, Astronomy and Informatics, Nicolaus Copernicus University, Grudziadzka 5, 87-100 Torun, Poland*
[22] *Department of Astronomy, University of Cape Town, Private Bag X3, Ronderbosch 7701, Cape Town, South Africa*
[23] *INAF - Istituto di Radioastronomia, via Gobetti 101, 40129 Bologna, Italy*
[24] *Astronomical Observatory Institute, Faculty of Physics, Adam Mickiewicz University, ul. Słoneczna 36, 60-286 Poznań, Poland*
[25] *East Asian Observatory, 660 N. Aohoku Place, University Park, Hilo, Hawaii 96720, U.S.A.*
[26] *Oxford Astrophysics, University of Oxford, Keble Rd, Oxford OX1 3RH, UK*
[27] *Department of Astronomy, Kyoto University, Kitashirakawa-Oiwake-cho, Sakyo-ku, Kyoto 606-8502, Japan*
[28] *Academia Sinica Institute of Astronomy and Astrophysics, 11F of Astronomy-Mathematics Building, AS/NTU, No.1, Section 4, Roosevelt Road, Taipei 10617, Taiwan*
[29] *Research Center for Space and Cosmic Evolution, Ehime University, 2-5 Bunkyo-cho, Matsuyama, Ehime 790-8577, Japan*

Accepted XXX. Received YYY; in original form ZZZ

ABSTRACT

We present an 850-μm mosaic map and extracted catalogue of submillimetre sources in the extended North Ecliptic Pole (NEP) region over about 2 deg^2. The 850-μm map is constructed using newly obtained observations by SCUBA-2 at the East Asian Observatory's James Clerk Maxwell Telescope, carried out using the observatory's large programme opportunities. The recent 850-μm survey has extended the submillimetre data coverage by almost a factor of 4 compared to previous surveys, with a depth of $\sigma_{\rm rms} = 1.0$–2.3 mJy beam^{-1}. The catalogue contains 549 sources selected above a significance level of 4σ, where the false-detection rate is 10 per cent; a higher threshold of 4.5σ is required in order to achieve a false-detection rate below 3 per cent, which results in 342 sources being selected. Despite the large spatial variation of the noise, the deboosted flux density of sources is comparable to results from the SCUBA-2 Cosmology Legacy Survey (S2CLS), which covered the central 0.6 deg^2 of our survey area with better sensitivity. We construct the source counts at 850 μm, finding results in agreement with other 850-μm surveys in cosmological blank fields over S_{850} = 4–15 mJy. We find a slight excess of bright galaxies ($S_{850} > 15$ mJy), which can be considered to be at $z_{\rm phot} = 2$–4. The 850-μm data adds valuable long-wavelength information to mid-infrared-selected sources from the *AKARI* NEP-deep and NEP-wide surveys, which will be helpful in preparing for future near-infrared to millimetre wavelength observations in the NEP region. Our 850-μm mosaic map and source catalogue will be made publicly available.

Key words: galaxies: evolution – submillimetre: galaxies – galaxies: photometry – galaxies: starburst

1 INTRODUCTION

Dust plays a significant role during the star-formation process by enhancing the formation of molecular hydrogen and the shaping of the spectral energy distributions (SEDs) of galaxies through absorbing UV photons from stars and re-radiating the energy in the rest-frame far-infrared. To obtain a complete picture of cosmic star-formation history and to understand the physical drivers of galaxy evolution, it is necessary to investigate the properties of dust in galaxies at different cosmic epochs. The selection of dusty galaxies generally utilises observations that sample rest-frame wavelengths above 100 μm, beyond the peak of the far-IR SED. Although the number density of star-forming galaxies selected in the rest-frame far-IR (i.e., 'dust-obscured' galaxies) is smaller than that of optically-selected populations, such as Lyman break galaxies, the high star-formation rates (SFRs) of IR-selected star-forming galaxies make these the most extreme star formers in the Universe (e.g., Whitaker et al. 2017; Hill et al. 2018). The contribution to the global cosmic SFR density by such obscured galaxies increases as we move to $z > 1$ (e.g., Le Floc'h et al. 2005; Magnelli et al. 2013) and the trend seems to remain out to $z \simeq 3$. The selection of obscured star-forming galaxies and their characterisation also provides an opportunity to investigate the most active regions of cosmic star formation at $z > 2$ (e.g., Casey, Narayanan and Cooray 2014).

It has been more than two decades since the so-called 'submillimetre' galaxy population (SMGs) was discovered, and it has subsequently been widely studied (e.g., Smail et al. 1998; Blain et al. 2002; Chapman et al. 2003). Follow-up studies showed that submillimetre (hereafter 'submm') galaxies are heavily obscured (Geach et al. 2007; Hainline 2008; Michałowski et al. 2010), gas-rich (Greve et al. 2005; Tacconi et al. 2006; Riechers et al. 2010; Toft et al. 2014), and massive (Hainline 2008; Michałowski et al. 2010, 2014; Smolčić et al. 2015; Dudzevičiūtė et al. 2020) galaxies located at a median redshift of $\langle z \rangle \simeq 2$–3 (Chapman et al. 2005; Pope et al. 2005; Smolčić et al. 2012; Simpson et al. 2014; Koprowski et al. 2016; Brisbin et al. 2017), covering the entire redshift range of $z = 1.5$–4 (Dudzevičiūtė et al. 2020; Simpson et al. 2020). The large total IR luminosities of SMGs (of order 10^{13} L$_\odot$) reflects SFRs as large as 100–1000 M$_\odot$ yr^{-1} (Magnelli et al. 2013; Barger et al. 2014; Toba et al. 2020), with massive SMGs constituting the upper end of the star-forming main sequence, while some less massive SMGs are located above the main sequence (Liu et al. 2019). Note, however, that the submillimetre fluxes of SMGs detected in single-dish observations could sometimes be overestimated by the blending of several sources within the large beam (e.g., Hwang et al. 2010; Hodge et al. 2013).

SMGs could also be associated with active galactic nuclei (AGN; Wang et al. 2013; Banerji et al. 2015; Toba et al. 2018; Ueda et al. 2018), complicating the relationship between SFR and submm flux. Nevertheless, the properties of SMGs suggest a scenario where they are strong candidates for being the progenitors of low-redshift massive elliptical galaxies (Simpson et al. 2017; Cooray 2019); this idea is also supported by simulations (Gonzalez et al. 2011; Toft et al. 2014). Overdensities of galaxies are often found around these SMGs (Menendez-Delmestre et al. 2013; Dannerbauer et al. 2014), and thus they provide an effective tool for tracing structures in the Universe. On the other hand, there is some doubt about whether the SMGs are good tracers of galaxy overdensities at $z \lesssim 3$, contrary to the case at $z \gtrsim 3$ (Miller et al. 2015; Smolčić et al. 2017). Because of this, selection and characterisation of the SMG population opens a window for studying key aspects of galaxy evolution, in terms of enhancing and quenching star formation, the growth of black holes along with stellar mass, and the formation of large-scale structures in the Universe. Since

⋆ E-mail: hjshim@knu.ac.kr

the investigation of the properties of SMGs requires well-defined multi-wavelength ancillary data sets, several wide-area submm/mm observations have been executed and these continue to be proposed and extended for several cosmological 'blank' fields.

Among the popular blank fields, the North Ecliptic Pole (hereafter NEP) region is a hub for existing and upcoming survey programmes using past, present, and future space telescopes, thanks to the high visibility of this region of the sky from their orbits. Multi-wavelength data over more than 4 deg^2 around the NEP have been accumulated, mostly based on the legacy survey of the infrared telescope *AKARI* (Matsuhara et al. 2006). The available data sets include observations covering UV, optical, mid- and far-IR, and radio wavelengths (e.g., Hwang et al. 2007; White et al. 2010; Kim et al. 2012; Pearson et al. 2012; Takagi et al. 2012; Oi et al. 2014; Nayyeri et al. 2018, Oi et al. 2020, submitted.; Kim et al. 2020, in prep.), while there are still a number of upcoming space-based surveys that have marked this region as one of the most advantageous fields for addressing multi-wavelength galaxy evolution. The X-ray telescope *eROSITA* plans to carry out an all-sky survey with the goal of finding rare populations of heavily dust-obscured AGN, while having its longest total exposure in the NEP region. *Euclid*, a space-based mission to map the dark-matter distribution of the Universe, based on weak-lensing and precise redshift measurements (Laureijs et al. 2011), will target the NEP as one of the three '*Euclid*-deep' fields to study numerous topics related to galaxy evolution. *SPHEREx*, an all-sky spectral survey mission in the near-IR, will provide a high cadence, deep survey in the NEP region. Both *Euclid* and *SPHEREx* will provide low-resolution spectra in the near-IR for most *AKARI* mid-IR-selected extragalactic objects. Such near-IR spectral information will be of particular use when combined with far-IR-to-submm surveys over a wide area in order to sample the dusty star-forming galaxy population out to high redshift.

With these scientific motivations in mind, we have pursued an 850-μm imaging survey in the NEP region with the Submillimetre Common User Bolometer Array-2 (SCUBA-2; Holland et al. 2013) on the James Clerk Maxwell Telescope, as part of the East Asian Observatory's (EAO's) large programmes. During three years of observation from 2017 to 2019, 200 hours of additional observations covered approximately 2 deg^2 at a shallower depth than that of the previously obtained 850-μm data over a much smaller area (0.6 deg^2; Geach et al. 2017). By combining the newly obtained data with the archival data, we have now doubled the number of submm sources above S_{850} = 6 mJy around the NEP. These submm sources can be studied through an SED-based analysis utilising the available rich multi-wavelength photometry. The SCUBA-2 850-μm survey of the NEP will continue after 2020, providing an opportunity to better constrain far-IR dust properties and AGN contributions for mid-IR-selected star-forming galaxies at different redshifts.

In this paper, we present the observations, data reduction and 850-μm source catalogue from our JCMT SCUBA-2 large programme to map a region around the NEP, based on the data obtained up until 2019. We also combined the archival data with newly obtained data to produce an improved 850-μm map. The paper is organized as follows. In Section 2, we describe our survey programme, including how the observations were made and how the data were reduced. We describe the construction of the 850-μm source catalogue in Section 3, along with estimations of flux deboosting, completeness, positional uncertainty and false detection rate, based on statistical simulations. In Section 4 we present 850-μm number counts, a brief introduction to the multi-wavelength identification of 850-μm sources, and the SEDs of the brightest sources, those having 850-μm flux density larger than 15 mJy. Finally we summarise our paper and provide conclusions in Section 5. Throughout the paper, we have explicitly assumed a WMAP 7-year cosmology (Komatsu et al. 2011). If a *Planck* 2018 cosmology (Planck Collaboration 2020) were to be used instead, the luminosities would be higher by 9 per cent at $z = 3$.

Table 1. Central coordinates of subfields in the NEPSC2 survey (JCMT program ID: M17BL007). The fourth column lists the 850-μm sensitivity measured in the centre of each subfield using the individual mosaic, i.e., without accounting for the overlap between subfields and with the S2CLS data.

Subfield	RA	Dec	1σ depth in the centre [mJy beam^{-1}]
NEP1	17 59 14.9	+66 53 58.9	2.2
NEP2	18 00 39.5	+66 29 36.6	2.3
NEP3	17 57 44.8	+66 08 56.4	1.9
NEP4	17 53 29.3	+66 13 25.0	2.0
NEP5	17 52 08.5	+66 38 34.1	2.1
NEP6	17 54 59.4	+66 58 27.9	2.1
NEP7	17 57 54.1	+67 18 42.8	2.2
NEP8	18 02 09.6	+67 14 13.9	2.2
NEP9	18 03 30.4	+66 49 30.4	2.5

2 OBSERVATIONS AND DATA REDUCTION

2.1 Observations

The NEPSC2 data presented in this publication were observed as part of JCMT program ID M17BL007. The data were obtained with the SCUBA-2 instrument (Holland et al. 2013) at 850 μm over the period from July 2017 to November 2019. In order to obtain 850-μm images over a wide (4 deg^2) area centred on the NEP (RA= $18^{\rm h}00^{\rm m}00^{\rm s}$, Dec= +66°33′38.5″), we used multiple 30-arcmin maps in a tiling pattern to provide even coverage, with each individual field referred to as a 'subfield'. Each 30-arcmin map, known as a PONG1800 map (Holland et al. 2013; Thomas & Currie 2014), provides uniform sensitivity in the inner circular region of 30 arcmin (1800 arcsec) diameter. Each PONG1800 observation took 40 minutes of on-sky integration time and each subfield was observed 28 times so that the total integration time for a single subfield was 18.7 hours.

Observations were executed in Grade 3 weather conditions, with a sky opacity at 225 GHz (τ_{225}) ranging between 0.08 and 0.12. The data quality was better when the observations were made with lower $\tau_{225\,\rm GHz}$ combined with higher elevation. Changes in subfield observing transmission (dependent on opacity and airmass) resulted in a variation in the 'depth' of the data for different subfields.

As of December 2019, observations of nine subfields (NEP1 to NEP9) have been completed, with approximately 170 hours of total integration time (Table 1). The actual time spent by the programme is longer, since there are some

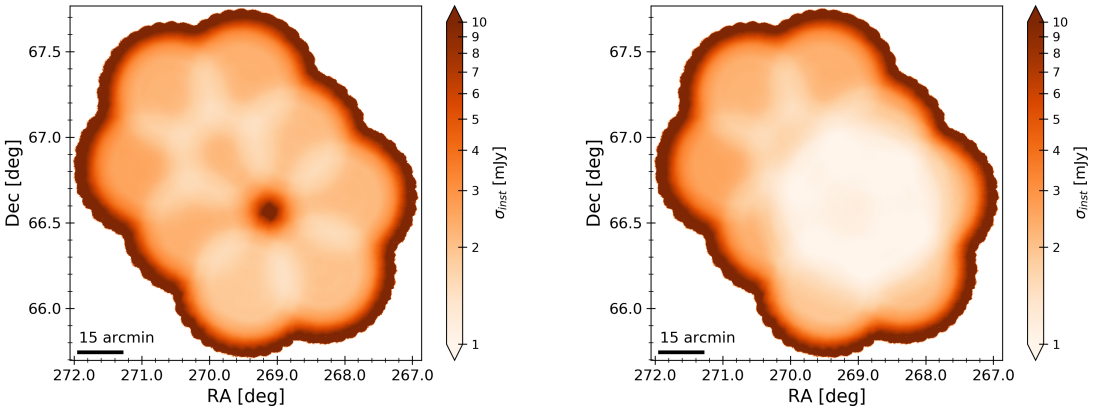

Figure 1. (Left) Noise map over the NEP field obtained through the JCMT large programme M17BL007, based on the data obtained between 2017 and 2019 (nine fields completed). The empty central region corresponds to the previous SCUBA-2 survey coverage (S2CLS; Geach et al. 2017), which is centred on the NEP itself. In the middle of each target field, the sensitivity ranges over σ = 1.9–2.5 mJy (Table 1); in its deepest region, where more than two subfields overlap, the map goes as deep as σ = 1.4 mJy. (Right) Noise map constructed by combining all new (NEPSC2; from M17BL007) and archival (S2CLS; from MJLSC02, Geach et al. 2017) SCUBA-2 850-μm observations over the NEP region. The previous S2CLS mosaic map has a mean sensitivity of $\langle\sigma\rangle$ = 1.2 mJy, while the deepest regions in the newly created map have a sensitivity of σ = 1.0 mJy.

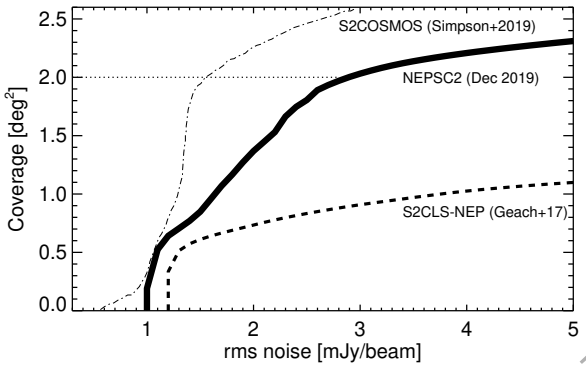

Figure 2. Cumulative areal coverage of 850-μm observations over the NEP region as a function of sensitivity. The y-axis indicates the area where the instrumental noise is less than the value $\sigma_{\rm rms}$. The S2CLS-NEP map (Geach et al. 2017) covered 0.6 deg^2 to a depth of 1.2 mJy rms (dashed line). With our new JCMT large programme, we have reached to $\sigma_{\rm rms} \simeq 1$ mJy in the overlapping regions, slightly deeper than the previous 850-μm data on the NEP. In addition to that, we have extended the 850-μm coverage to 2 deg^2 (horizontal dotted line), while our source-extraction procedure (Section 3) allows for the detection of sources in the shallower region at the S/N > 4 detection level. For comparison, we have overplotted with a dot-dashed line the area as a function of noise from the S2COSMOS survey (Simpson et al. 2019).

subfields that were observed only a few times and are not included in this work. Table 1 lists the central coordinates of the nine subfields. The effective survey area is 1.7 deg^2, without accounting for the previously existing S2CLS data (JCMT program ID MJLSC02), where the sensitivity level is quite different. The combined noise map (of the subfields for NEP + S2CLS) is shown in Fig. 1. In the centre of each subfield, the sensitivity ranges between 1.9 and 2.5 mJy beam^{-1} rms (Table 1), mainly depending on the weather conditions and field elevation at the time of the observations. It can be seen that the sensitivity is better in the overlapping region between tiles. The deepest region, in the combined map of NEP and S2CLS, has a sensitivity of 1 mJy beam^{-1}. Figure 2 shows the cumulative areal coverage of the 850-μm data over the NEP that is deeper than a given sensitivity. Previously available 850-μm data in the NEP obtained as part of the S2CLS project (Geach et al. 2017) provides a uniform sensitivity of 1.2 mJy rms in the central 0.6 deg^2. With the new data obtained through NEPSC2, the coverage has been extended to 2 deg^2 (although the actual effective survey area is dependent on the sensitivity threshold) and the noise level has reached down to 1 mJy rms in the deepest region. Currently the areal coverage of the NEPSC2 survey is still smaller than that of the S2COSMOS project (Simpson et al. 2019), which provides uniform sensitivity over 2 deg^2. The observations are expected to be completed by 2022 through the recently approved large programme extension; we will then have approximately 4 deg^2 coverage with a sensitivity comparable to that of the currently existing data.

2.2 Data reduction

We used the ORAC-DR data reduction pipeline (Cavanagh et al. 2008), which is an automated process that follows pre-defined recipes to produce calibrated flux-density maps from the obtained data frames. The SCUBA-2 850 μm array is made up of four sub-arrays, and records a time-varying signal that is a sum of contributions from astronomical sources, background (mostly from sky emission) and noise (Holland et al. 2013). The data reduction is based on extracting the signal from astronomical sources, and producing a two-dimensional (spatial) flux-density map projected onto the celestial sphere. The SCUBA-2 data reduction pipeline is equipped with the Dynamical Iterative Map-Maker (DIMM) within the Sub-Millimetre Common User Reduction Facility (SMURF), which performs the removal of contaminating signal components and carries out the map production (see Chapin et al. 2013 for details).

The parameters we used are consistent with those proposed for 'blank-field' data reduction (Geach et al. 2017), which aims to detect low signal-to-noise ratio (S/N) point sources from deep-field observations. The configuration file is included in the data reduction pipeline distribution as *dimmconfig_blank_field.lis*.

The data reduction process uses the following set of procedures. The raw time-series data are read and resampled at a 2-arcsecond pixel scale within the pipeline, followed by a number of cleaning steps. Flat fields are applied using the associated flat scans, and a polynomial baseline fit is subtracted from each sub-array. Then the pipeline begins an iterative process that attempts to fit the data with a model comprising several components: a common-mode background signal from the atmosphere; the astronomical signal; and noise (accounting for both instrumental noise and fine-scale atmospheric noise). The iteration is performed until the maximum number of iterations is reached or if the result converges. As is suggested in the distributed configuration file (*dimmconfig_blank_field.lis*), we repeat the iteration four times.

For flux calibration, we apply flux-conversion factors (FCFs) to the data frames in order to convert the data from pW to units of Jy beam^{-1}. We explicitly used the recently released (30 January 2020) values of FCF[1] tabulated in bins of ($\tau_{225\mathrm{GHz}}$×airmass) for the time the observation was made. The mean value of the FCFs applied to each scan was comparable to the historical reference value (Dempsey et al. 2013), which was used in reducing S2CLS data.

After all scans were reduced and flux calibrated, the final mosaiced map was produced with the PICARD recipe *mosaic_jcmt_images*. We combined all scans in different subfields simultaneously, weighting each input image by the inverse variance per pixel. To optimize (faint) point-source detection, we applied a matched filter (PICARD recipe *scuba2_matched_filter*) to the map by convolving a Gaussian kernel that matches the instrumental point-spread function, i.e., with a 15 arcsec FWHM Gaussian. Previous work (e.g., Geach et al. 2017) on the matched-filter application to the SCUBA-2 maps suggested that a slight loss (of order of 10 per cent) in the response is expected during the filtering process. In order to estimate the flux loss, we inserted bright (20–50 mJy) artificial point sources of known flux density into the map, using the 15 arcsec FWHM at 850 μm. Then by recovering their flux densities before and after the matched-filtering, we estimated the flux loss rate to be 5 per cent and subsequently corrected the flux map by this factor.

3 SOURCE EXTRACTION

Essentially all submm galaxies can be considered to be unresolved sources given the SCUBA-2 resolution, except some galaxies at very low redshifts. Therefore the peak value in a beam-convolved map can be taken to be the flux density of the extracted source. We extract the sources with a simple top-down peak-finding method that has been widely adopted in other submm surveys of cosmological fields (e.g., Pope et al. 2005; Coppin et al. 2006; Geach et al. 2017; Simpson et al. 2019). We first find the most significant peak in the S/N map, then store the peak flux, noise, and position in the catalogue. Once the information has been recorded, the source is removed from both the S/N map and the flux map by subtracting a scaled version of the model point-spread function. The point-spread function (PSF) we use is constructed by coadding all $> 5\,\sigma$ point sources in the map. Like in previous works (Geach et al. 2017; Simpson et al. 2019), the empirical PSF shows a negative ring as a result of the matched filtering, and has a FWHM of 14.9 arcsec. The peak-finding procedure effectively 'deblends' in a way that is essentially the same as PSF-fitting. The source-finding steps are repeated to reach down to the specific detection-limit floor, in our case 3σ, which means the detection iteration process for exploring the lowest significance detections stops when we have reached 3 times the background rms level.

When another source is found within 7.5 arcsec of any source found in the previous run, we consider that these two sources are the same. This avoids too much fragmentation that would artificially arise within the dark ring area produced by matched filtering. Even with this strategy, no sources in the final catalogue turned out to be spatially extended, and all are consistent with being point sources. Our final catalogue includes sources with S/N > 4 (i.e., $4\,\sigma$ detection threshold). However, as we will discuss in Section 3.4, considering the false-detection rate, it would be safer to place a higher detection limit (such as $4.5\,\sigma$, to give a false-detection rate lower than a few per cent) for a robust catalogue of submm sources.

3.1 Completeness and flux boosting

Statistically speaking, flux densities of submm sources selected using a threshold tend to be 'boosted'. The simplest form of boosting is called Eddington-type bias (Eddington 1913), which is the effect on number counts due to the statistical variation around the true flux densities of sources. Since fainter sources are more numerous than brighter ones, then at a given measured flux level it is more probable to find faint sources scattering up than bright sources scattering down. Another effect on flux boosting comes from source confusion. Objects below the detection threshold contribute to the measured flux density, increasing the observed flux density compared to the intrinsic value. Flux-boosting factors, representing a combination of the two effects, can in general be described as a function of both signal and noise (Coppin et al. 2005; Casey et al. 2013; Geach et al. 2017), with the highest S/N sources being relatively unaffected by flux boosting. For NEPSC2 850-μm data, we evaluated the magnitude of the flux boosting as a function of the local noise level and the observed flux density, based on the empirical approach described in Geach et al. (2017).

We constructed a jackknife noise map for use in this analysis. The individual scans were randomly divided into two subgroups, to produce separate mosaic images for each of these two subgroups. Then we subtracted one mosaic from the other and scaled the result in terms of the square root of total integration time. In this 'source-free' noise map, artificial sources with known flux densities and positions were injected. The source extraction procedure was performed on the simulated flux map to quantify how many injected

[1] https://www.eaobservatory.org/jcmt/instrumentation/continuum/cuba-2/calibration/

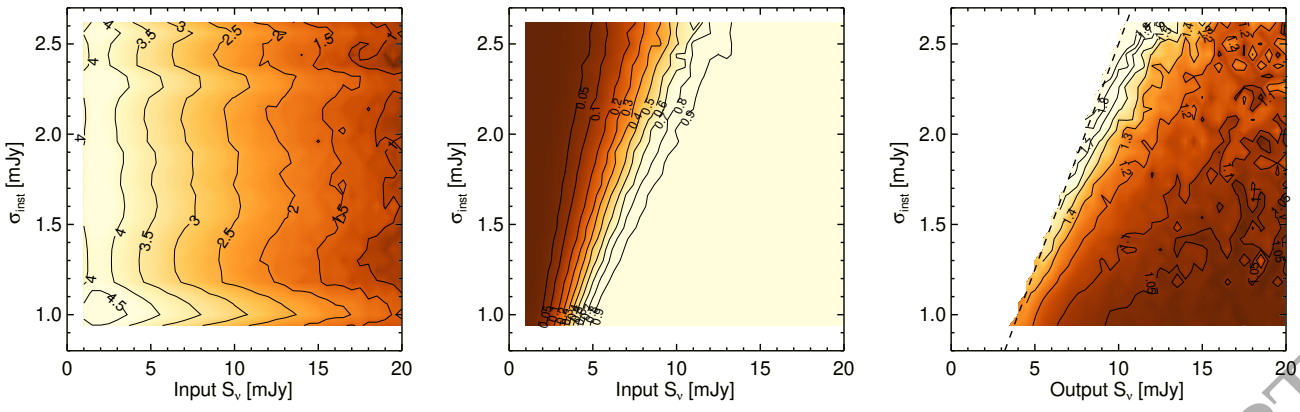

Figure 3. Visualisation of results from simulations of the recovery of sources in the two-dimensional space of flux density and uncertainty. The left panel shows the number of artificial sources injected into the jackknife mosaic map per bin of input flux density and instrumental noise. The annotated numbers indicate $\log_{10} N_{\rm injected}$. The middle panel shows the completeness, i.e., the number of recovered sources divided by the number of injected sources, as a function of input (intrinsic) flux density and the instrumental noise. The right panel shows the average boosting factor for the output (observed) flux density and the instrumental noise. The dashed line indicates the $4\,\sigma$ limit applied in the source-extraction procedure.

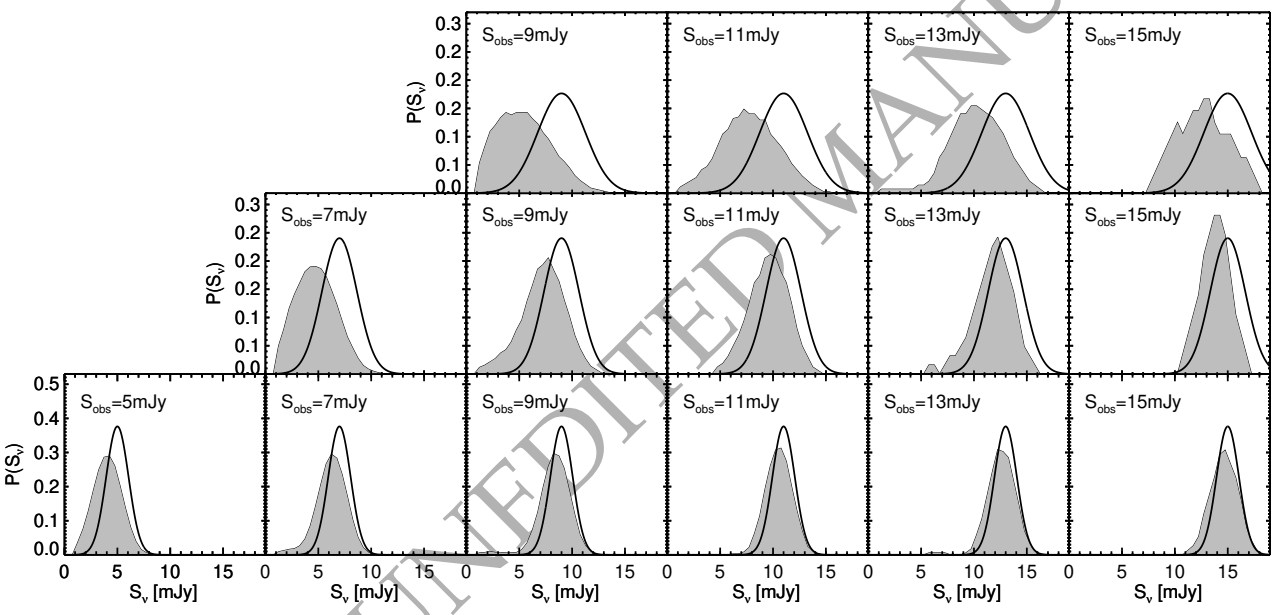

Figure 4. Deboosted (intrinsic) flux-density distribution based on the empirical recovery method (filled distribution), compared to the observed flux-density probability distribution assuming Gaussian uncertainties (open distribution). The observed flux densities increase from left to right panels. The top row shows distributions measured when $\sigma_{\rm inst} = 2.2$ mJy, the middle row shows results for $\sigma_{\rm inst} = 1.6$ mJy and the bottom row shows results for $\sigma_{\rm inst} = 1.0$ mJy. The ratio between the peaks of two (observed and intrinsic) distributions is considered to be the boosting factor.

sources were recovered (an estimation of survey completeness) and how their flux densities compared with the intrinsic values (an estimation of flux boosting). We found that the flux distribution of sources inserted into the noise map follows the observed number counts fit from Geach et al. (2017), which has the form of a Schechter function:

$$\frac{dN}{dS} = \left(\frac{N_0}{S_0}\right)\left(\frac{S}{S_0}\right)^{-\gamma} \exp\left(-\frac{S}{S_0}\right), \quad (1)$$

where N is the number of sources and S is the flux density, with $N_0 = 7180\,\mathrm{deg}^{-2}$, $S_0 = 2.5$ mJy, and $\gamma = 1.5$. The range of flux densities of inserted sources was 1–50 mJy. Each source was placed in a random position, assuming a spatially uniform distribution (i.e., we did not consider any clustering effects). An inserted source is considered to be recovered if a point source is found above the detection threshold within 1.5×FWHM of the input position. If there are multiple matches, we took the nearest one. Source extraction was

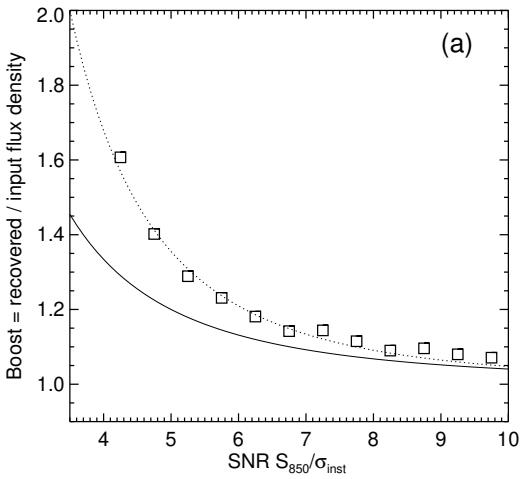

Figure 5. (Left) Average flux-boosting factor as a function of signal-to-noise ratio. The boosting is well described by a power law (dotted line, equation 2); however, in practice, we estimated boosting in the two-dimensional parameter space composed of observed flux density and instrumental noise. The average boosting factor described as a power law by Geach et al. (2017) is overplotted as a solid line. (Right) Average positional uncertainty, defined as the difference between the input and recovered positions, as a function of the signal-to-noise ratio. As in previous studies (solid line from Geach et al. 2017; dashed line from Ivison et al. 2007), and as in the case for flux boosting, the positional uncertainty is well described by a power law (dotted line, equation 3). Such positional uncertainties need to be considered in the identification process for the 850-μm sources in data at other wavelengths.

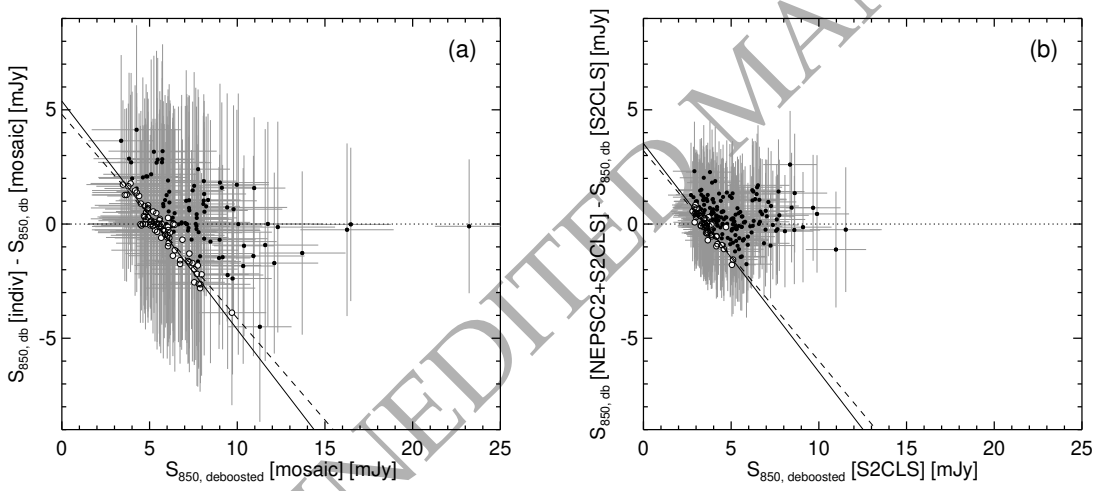

Figure 6. Comparison between the flux densities of sources measured in different images. The left panel shows a comparison between the deboosted flux densities of sources measured in the maps of individual target subfields and in the entire mosaic map, which has better sensitivity where the pointing tiles overlap. The y-axis shows the difference between the two measurements (plotted as filled circles). Open circles are sources between 4 and 4.5σ, suggesting that the apparent boundary from upper left to lower right is due to the detection limit imposed by the 4σ detection at $\sigma_{\rm rms}$ = 1.4 mJy. The dashed and the solid lines show linear fits that describe the flux difference as a function of flux, with varying slopes and using a fixed slope of −1, respectively. Despite the background noise fluctuations, the flux densities measured in the two maps show overall agreement within the flux density uncertainties. The right panel shows a comparison between the deboosted flux densities, measured in the previous S2CLS map (Geach et al. 2017; limited to the central 0.6 deg^2 region of the NEP) and in our new 850-μm mosaic map. This panel contains 222 sources that are cross-matched between the two catalogues. As in the left panel, open circles are sources between 4 and 4.5σ in the [NEPSC2+S2CLS] map. The dashed and the solid lines show the linear fits with varying and fixed slopes (of −1), respectively.

performed in exactly the same way as for constructing the source catalogue from the observed flux map, which means the extraction is a blind detection, not using the expected source position as a prior. By combining many noise maps with many artificial source catalogues, we generated 2500 sets of mock catalogues that contain matched information for 2×10^5 sources. Based on these results, we assessed the completeness and flux-boosting statistics.

Figure 3 summarises the recovered sources in the two-dimensional plane of local instrumental noise (i.e., the ob-

served flux uncertainty) and flux density. The left panel shows that there is an enhancement in the number of injected sources for a range of values of instrumental noise, e.g., note the horizontal concentration at $\sigma_{\rm inst}$ = 1.0 and $\sigma_{\rm inst}$ = 2.3 mJy. This reflects the different sensitivity levels depending on location in the map. The completeness, illustrated in the middle panel, is defined as the ratio between the number of recovered sources and the number of total injected sources. For regions with the lowest noise levels ($\sigma_{\rm inst} \simeq 1$ mJy), the 50 per cent completeness limit is 3.9 mJy and the 80 per cent completeness limit is 4.7 mJy. In the regions where different subfields do not overlap ($\sigma_{\rm inst} \simeq$ 2.3 mJy), the 50 and 80 per cent completeness limits are 8.5 and 11 mJy, respectively.

By comparing the 'recovered' flux densities to the input flux densities, the amount of flux boosting can be evaluated as a function of noise and observed flux density. A source with observed flux density $S_{\rm obs}$ is actually drawn from the probability distribution of its true flux density, $p(S_{\rm true})$. A histogram of injected source flux densities in bins of ($S_{\rm obs}$, σ) is considered to be an estimate of $p(S_{\rm true})$. Examples of evaluating $p(S_{\rm true})$ are shown in Fig. 4. The observed flux-density distribution is assumed to be a Gaussian, with an FWHM identical to that of the local instrumental noise. The mean and the variance of the intrinsic flux distribution $p(S_{\rm true})$ provides the boosting factor and the uncertainty in the deboosted flux density. The boosting factor is smaller when the observed flux density is high and the noise level is low. The uncertainty on the deboosted flux density ($\sigma_{\rm deb}$) is quadratically added to other uncertainties (instrumental noise and confusion noise) to produce the total flux error in the source catalogue (see Table 2). In our constructed two-dimensional grid of boosting factors (Fig. 3 right panel), we derive a boosting factor for each source based on a two-dimensional spline interpolation, using the binned values as a look-up table. The average flux boosting factor $\mathcal{B}$ can be described as a power-law function of S/N (Fig. 5a):

$$\mathcal{B} = 1 + 0.3 \times \left(\frac{\rm S/N}{5.3}\right)^{-2.9}. \quad (2)$$

We also plot the equivalent relation from S2CLS survey (equation 5 of Geach et al. 2017) in Fig. 5a for comparison. While both lines have similar forms, i.e., the boosting factor is proportional to a power of S/N, our recovery simulations suggest that larger boosting is expected in the NEPSC2 mosaic than in the average S2CLS map. This difference is due to the fact that the typical noise level of NEPSC2 are larger than those of S2CLS. Geach et al. (2017) showed that at a fixed S/N, the average boosting factors are similar across different fields. However, in the lower S/N regime, approximately 10 per cent difference in boosting was seen between the deeper S2CLS fields (e.g., UKIDSS-UDS; σ = 0.9 mJy beam^{-1}) and the shallower S2CLS fields (e.g., COSMOS; σ = 1.6 mJy beam^{-1}). Therefore relatively large deboosting corrections are required for sources extracted from the shallow (up to σ = 2.2–2.5 mJy beam^{-1}) part of the NEPSC2 map; this can be seen from the large deviation between our results and those from Geach et al. (2017) at S/N below 4 (Fig. 5a). In Section 3.3 we will show a source-by-source flux comparison between our work and the previous S2CLS-NEP study.

3.2 Positional uncertainty

Simulations also allow us to estimate the differences between inserted positions and recovered positions. We measure the average offset $\delta\theta$ between input and recovered position in bins of flux density and local instrumental noise. The quantity $\delta\theta$ is calculated based on the conventional way to estimate separation between two positions projected on to the sky: we know the right ascension and declination of each injected source, while its observed right ascension and declination are measured during the source extraction process. The quadratic sum of right ascension difference multiplied by cos(declination) and the declination difference is defined as $\delta\theta$, and interpreted as the positional uncertainty.

The positional uncertainty of 850-μm sources, which should be used for multi-wavelength counterpart identification, increases for objects with low S/N (see Fig. 5b). Geach et al. (2017) suggested that the positional uncertainty $\delta\theta$ can be described as a power-law function of S/N (equation 6 of Geach et al. 2017; equation B22 of Ivison et al. 2007). We found similar power-law relation between $\delta\theta$ and S/N as follows:

$$\delta\theta = 1.4\,{\rm arcsec} \times \left(\frac{\rm S/N}{9}\right)^{-0.9}. \quad (3)$$

Overall, our positional uncertainty at a fixed S/N is a little larger than that from the S2CLS survey, but is comparable to the expression suggested by the earlier study of Ivison et al. (2007), when power law of the source count distribution is assumed to be β = 2.8 and the FWHM is 15 arcsec. Simpson et al. (2019) for S2COSMOS, also reported that positional uncertainties of 850-μm selected sources are similar to our results, based on source-recovery simulations. In S2COSMOS, the median positional uncertainty for 4σ source extraction is around 3 arcsec, while most sources are recovered with offsets less than 8.7 arcsec. Based on preliminary counterpart identification using 1.5-GHz Karl G. Jansky Very Large Array (VLA) data, we found that around 80 per cent of the 850-μm sources in the NEPSC2 catalogue that are identified in the 1.5-GHz image have offset smaller than 3 arcsec. Note that the typical positional offset between objects at different wavelengths may not be applicable when 850-μm sources are blends of multiple sources.

3.3 Verification of the flux deboosting

We extracted sources from the mosaic map covering the entire NEP (see Fig. 1), which is produced by combining all the existing observations including S2CLS data and the nine newly observed subfields. It is also possible to produce flux maps for each subfield separately, to obtain a circular field with uniform depth. Source extraction can be performed on each of these. In the case of sources lying in the overlap region, the observed flux densities in the former map (i.e., the mosaic map covering the entire field) and in the latter map (i.e., a map of an individual subfield) might be different due to differences in the local noise levels. Since we used a two-dimensional parameterisation to evaluate flux boosting, the deboosted flux densities should be consistent for the same

source. Figure 6a shows such a comparison between the deboosted flux densities of the same sources in two distinct maps. There is an apparent boundary due to the 4σ source selection threshold, yet no trend is seen for flux differences in terms of the observed flux. Except for a small number of outliers, the deboosted flux densities of the same source are consistent, within the total flux errors. The few outliers tend to be located near the edge of the individual subfield map, thus making source extraction more challenging because of the increased noise level.

We cross-matched our catalogue with the S2CLS catalogue (Geach et al. 2017) by using a search radius of 7.5 arcseconds, and found 222 matches. The S2CLS catalogue contains 330 sources in the NEP region with a S/N threshold of $3.5\,\sigma$, which is lower than our level of $4\,\sigma$. In order to understand whether the failure of finding matches for 108 sources in the S2CLS catalogue is due to our S/N cut, we constructed a source catalogue from our updated mosaic map using a 3σ detection level and performed cross-matching with the S2CLS catalogue. Among the 108 sources, four are found very close (within 60 arcsec, i.e., 4 times the FWHM) to the dark ring around the bright Galactic source NGC 6543 caused by the matched filtering, so it is likely that they are artefacts from the data reduction (even though these are also detected in our map). 82 sources are detected in the new mosaic map with S/N values between 3 and 4, among which 62 sources were originally detected with $3.5 < \mathrm{S/N} < 4$ in the S2CLS catalogue, while 20 sources were reported to have S/N larger than 4. The remaining 22 sources in the S2CLS catalogue are 'not detected' in our mosaic, even with the lower S/N cut (3σ). The S2CLS catalogue shows that most of these 22 sources have estimated S/N less than 4. The number of missed sources in the new mosaic map, 22, is comparable to the expected number of false detections for a threshold of S/N = 4 in the S2CLS catalogue (7 per cent of 330 sources; Geach et al. 2017). Interestingly, there is one fairly bright source in the S2CLS catalogue (S2CLSJ175417+664913, $S_{850}^{\mathrm{deb}} = 21.5$ mJy) that completely disappears in our 850-μm mosaic map. When we construct a mosaic map using archival data only, we find no source at the position of S2CLSJ175417+664913. The reason for this source being detected in the S2CLS map and being missed in our map needs further investigation.

The deboosted flux densities of 222 matches between the S2CLS and our catalogue show good agreement (Fig. 6b), with an average flux-density difference of less than 20 per cent.

3.4 False-detection rate

In the low S/N regime, background fluctuation may lead to 'false detections'. To estimate the false-detection rate as a function of S/N, we compared the number of detections in the source-free jackknife noise map to the number of detections in the real flux map, using the same source-extraction method. The false-detection rate is defined as the ratio between these two numbers. Figure 7 shows that with our $4\,\sigma$ detection limit, the integrated false-detection rate is about 10 per cent. In the lowest S/N bin, at S/N = 4–4.2, the false-detection rate is as high as 20 per cent. If we were to adopt a higher S/N cut of $4.5\,\sigma$ for source detection, the integrated false-detection rate becomes approximately 3 per cent.

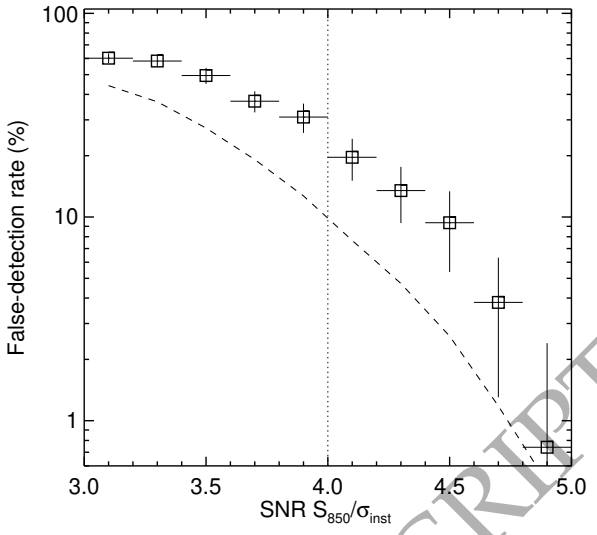

Figure 7. False-detection rate, defined as the ratio between the numbers of extracted sources in the jackknife noise map and the flux density map per signal-to-noise bin. The data points show the false-detection rate in the specific S/N bin, while the dashed line shows the 'integrated' false-detection rate, derived from the false-to-positive source number ratio above the fixed S/N limit (i.e., the false-detection rate measured above each > S/N value). At our S/N threshold of 4, we expect around 10 per cent false detections. The false-detection rate decreases to below 3 per cent if we adopt a 4.5σ threshold. Caution should be exercise when using objects with S/N between 4 and 4.5, since around 10 per cent of such sources are likely to not be real (or to be substantially fainter than the measured value).

Instead of applying the stricter $4.5\,\sigma$ limit, which would guarantee less than 3 per cent false detections, we include 4–$4.5\,\sigma$ sources as well in the source catalogue, since the vast majority of the additional sources are still real (and therefore interesting to follow up). However, when using the source catalogue (Table 2), the sources with S/N between 4 and 4.5 should be considered with some care. Multi-wavelength counterpart identification of the 850-μm sources will be important to judge whether an individual source is real or not. Work on the cross-identification of 850-μm-selected submm galaxies in near-IR/mid-IR/radio images, and the subsequent determination of their physical characteristics will be presented in a separate paper (Lee et al., in prep.). However, some results for the brightest sources are included in this paper, in Section 4.3.

3.5 Source catalogue

The final source catalogue contains 549 sources detected above 4σ over the approximately 2 deg^2 region around the NEP. The first ten catalogue entries are presented in Table 2. We list source IDs based on the coordinates, the positions of 850-μm sources, the observed flux densities with instrumental noise, the signal-to-noise ratios and the deboosted flux densities of sources with total flux uncertainty. The total flux uncertainty is a quadrature sum of the instrumental noise, confusion noise (0.8 mJy beam^{-1} at 850 μm), and the deboosting uncertainty, which is estimated from the intrin-

Table 2. 850-μm source catalogue from the NEPSC2 survey covering approximately 2 deg^2. Presented here are the first 10 rows of the catalogue, sorted in order of the observed flux density. The first source is NGC 6543, a Galactic planetary nebula. The first column indicates the IDs of each source, while the second and third columns give the (J2000) right ascension and declination, respectively. The column $S_{850}^{\rm obs} \pm \sigma_{\rm inst}$ is the observed flux density and instrumental noise, while S/N gives the signal-to-noise ratio of the detection. The column $S_{850}^{\rm deb} \pm \sigma_{\rm tot}$ gives the 'deboosted' flux density (which is an estimate of the intrinsic flux density), and the total uncertainty. The total uncertainty is the quadrature sum of the instrumental noise, confusion noise and deboosting error. The columns $\mathcal{C}$ and $\log_{10}\mathcal{F}$ are the completeness and false-detection rate corresponding to each source. The completeness $\mathcal{C}$ is estimated in the parameter space of ($\sigma_{\rm inst}$, $S_{850}^{\rm deb}$) presented in Fig. 3. The false-detection rate is estimated based on the S/N (Fig. 7). The last column gives the positional uncertainty for each 850-μm source (Section 3.2); this can be used for multi-wavelength catalogue cross-matching. The full catalogue will be released in the online version of the journal.

ID	RA	Dec	$S_{850}^{\rm obs} \pm \sigma_{\rm inst}$ [mJy]	S/N	$S_{850}^{\rm deb} \pm \sigma_{\rm tot}$ [mJy]	$\mathcal{C}$	$\log_{10}\mathcal{F}$	$\delta\theta$ [arcsec]
NEPSC2_J175833+663758	17 58 33.4	+66 37 58.5	195.9 ± 1.0	191.2	195.1 ± 1.4	1.00	−664.65	0.09
NEPSC2_J175052+660458	17 50 52.9	+66 04 58.1	35.6 ± 3.0	11.9	32.0 ± 3.1	1.00	−76.83	0.54
NEPSC2_J175244+660834	17 52 44.1	+66 08 34.2	23.5 ± 1.7	13.8	23.2 ± 2.0	1.00	−33.75	0.95
NEPSC2_J180330+664811	18 03 30.7	+66 48 11.9	20.2 ± 2.5	8.1	16.3 ± 2.7	0.99	−13.56	1.54
NEPSC2_J175846+671948	17 58 46.4	+67 19 48.7	18.8 ± 2.1	9.0	16.5 ± 2.3	1.00	−16.86	1.39
NEPSC2_J180002+673402	17 57 59.1	+67 24 21.7	14.9 ± 2.3	6.5	12.3 ± 3.3	0.95	−7.92	1.87
NEPSC2_J175515+664355	18 00 08.5	+67 13 30.3	14.7 ± 1.6	9.5	13.7 ± 2.5	1.00	−18.43	1.34
NEPSC2_J175518+663359	18 04 57.7	+67 15 42.0	14.6 ± 2.7	5.4	10.6 ± 4.1	0.65	−3.97	2.21
NEPSC2_J175426+655504	17 54 45.1	+65 59 20.4	14.1 ± 2.2	6.4	11.6 ± 3.0	0.95	−7.52	1.90
NEPSC2_J175448+663448	17 57 21.0	+65 55 38.6	14.0 ± 2.0	7.1	11.7 ± 3.2	0.99	−10.01	1.73

Table 3. Number counts measured in the 2 deg^2 mapped region of the NEP field. Here the flux density S is the bin centre, while the half-width of the flux density bin is ΔS = 0.5 mJy, and S' indicates $S' = S - \Delta S$. The uncertainties in number counts are standard deviations from the number-count estimates in each flux density bin from 1000 realisations, where each source is flux-deboosted assuming a deboosting probability distribution for the observed source flux density and instrumental noise, corrected for completeness and false-detection rate.

S [mJy]	dN/dS [deg^{-2} mJy^{-1}]	$N(>S')$ [deg^{-2}]
4.5	171.4 ± 21.0	391.5 ± 26.4
5.5	97.5 ± 14.6	223.1 ± 19.6
6.5	54.7 ± 10.7	127.5 ± 14.5
7.5	30.9 ± 8.3	73.5 ± 11.3
8.5	17.8 ± 6.5	42.7 ± 8.8
9.5	10.5 ± 5.3	24.7 ± 6.8
10.5	6.0 ± 4.2	14.4 ± 5.3
11.5	3.4 ± 3.4	8.4 ± 4.1
12.5	1.9 ± 2.7	5.1 ± 3.2
13.5	1.1 ± 2.2	3.5 ± 2.6
14.5	0.6 ± 1.8	2.7 ± 2.2

sic flux-density distribution (i.e., the standard deviation in Fig. 4). The completeness $\mathcal{C}$ (see Fig. 3 middle panel), and the logarithmic value of the false-detection rate $\mathcal{F}$ (at the specific S/N bin, see data points in Fig. 7) are also listed. Note that sources with S/N < 4.5 should be used with care, since the false-detection rate is non-negligible, as discussed in Section 3.4. Positional uncertainties derived using equation 3 are included in the source catalogue to help readers who want to cross-match the 850-μm source catalogue with catalogues at other wavelengths.

4 DISCUSSION

4.1 850-μm number counts

The surface number density of sources per flux density bin for a galaxy population is a simple measure of a specific population's abundance and provides a powerful tool for testing galaxy formation models through the comparison of the models with observations. The estimated number counts tend to be better constrained if the survey area is larger, because large areas are relatively free of excess variance due to clustering. Simpson et al. (2019) demonstrated that by constructing number counts in the separate sub-fields of the S2COSMOS survey (covering 1.6 deg^2), degree-scale fields are sufficiently wide to overcome the clustering effect for the flux range of 2–10 mJy. From the wider and shallower S2CLS survey, covering about 5 deg^2 in total (Geach et al. 2017), a similar conclusion has been reached, namely that the number counts from various fields generally agree to within 50 per cent in 0.5–1 degree fields, except for a marginal overdensity observed in a particularly small field (GOODS-North, 0.07 deg^2).

The 850-μm data in the NEP field are shallower than in some previous cosmological surveys already mentioned; this is especially true for the 'extended' fields where the median depth is $\langle\sigma_{\rm rms}\rangle$ = 2.3 mJy beam^{-1}. Furthermore, the coverage of the NEP SCUBA-2 survey is not the widest amongst cosmological fields that have been surveyed. As a result, our survey has limitations when it comes to improving constraints on the faint (as well as the bright) end of the 850-μm number counts. Nevertheless, the 850-μm number counts in the NEP region provide an independent test of whether the previously claimed statement is correct that degree-scale surveys are largely free of clustering effects. Wide surveys are also a way to search for rare populations of extremely bright 850-μm sources that are either lensed galaxies or highly confused sources from faint galaxy overdensities (Negrello et al. 2010; Vieira et al. 2010; Wardlow et al. 2013). Both scenarios for bright 850-μm sources are worthy of investigation in

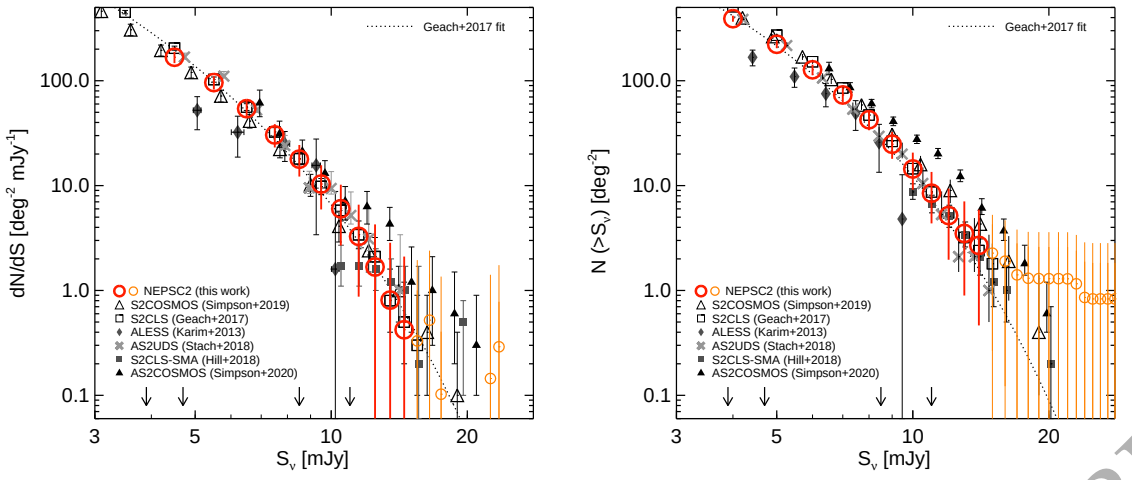

Figure 8. Differential (left) and cumulative (right) number counts of 850-μm sources in the 2 deg^2 around the NEP (open circles). One Galactic source (the Cats Eye Nebula NGC 6543, S_{850} = 195 mJy) is excluded. Number counts are corrected for the completeness and false-detection rates of individual sources. Our results are in good agreement with those from previous single-dish observations of cosmological blank fields (e.g., S2CLS, Geach et al. 2017 and S2COSMOS, Simpson et al. 2019) at S_{850} = 4–15 mJy. Number counts from higher-resolution interferometric observations (ALMA, SMA) are overplotted for comparison (Karim et al. 2013; Stach et al. 2018; Hill et al. 2018; Simpson et al. 2020). Arrows mark 3.9 and 4.7 mJy, which are, respectively the 50 and 80 per cent completeness limits for regions with σ = 1 mJy. For regions with σ = 2.3 mJy, source extraction is 50 and 80 per cent complete at 8.5 and 11 mJy. At the bright end, four 850-μm sources brighter than 15 mJy produce an excess (orange open circles) over the Schechter function fit (dotted line) presented by Geach et al. (2017).

terms of studying galaxy cluster-scale structures at different redshifts with good supporting multi-wavelength survey data.

To construct number counts, we used 548 sources in the catalogue, excluding one known Galactic source, the planetary nebula NGC 6543. For the differential number counts, the number of sources with deboosted flux within the flux density bin was converted to surface density (in units of deg^{-2} mJy^{-1}) using the areal coverage corresponding to the noise level where the source was detected. A completeness correction was applied to every source based on the corresponding completeness value derived from the simulations described above (Section 3.1). Each source was also corrected for the possibility of false detection (Section 3.4), by multiplying by (1−false-detection rate) before counting. The number count in a given flux density bin was calculated as follows:

$$\frac{dN}{dS} = \sum_i \left(\frac{1}{\Omega\,(>\sigma_i)}\right) \frac{(1-\mathcal{F}_i)}{C_i}, \qquad (4)$$

where $\Omega\,(>\sigma)$ indicates the areal coverage where the sensitivity is better than the observed flux uncertainty (see Fig. 2). The quantities $\mathcal{F}$ and C are the false-detection rate and completeness, respectively.

Uncertainties in the deboosted flux will contribute to uncertainties in the number counts. In order to take this effect into account, we generated 1000 catalogues of 850-μm sources by varying the intrinsic flux densities of individual sources according to the flux density distribution, i.e., the mean of 1000 cases being the deboosted flux density in the actual data catalogue (Table 2) and the standard deviation being the total flux uncertainty. Then number counts were calculated 1000 times using 1000 catalogues. Finally the mean and standard deviation of the 1000 realisations were taken as the final values for number counts and uncertainties, respectively. One of the advantages of this approach is that we obtain a continuous trend of number counts despite the small number statistics in some of the flux bins. In addition to the differential number counts, we also constructed the cumulative counts, which represent the surface number density of sources above each flux density; this provides a quantification of the total number of sources that will be selected in a flux-limited survey. The method for generating the cumulative counts is the same as the method used in calculation of differential counts. The results are summarised in Table 3 and Fig. 8. Although our source catalogue contains sources as faint as S_{850} = 2.8 mJy, we only present number counts for flux density bins brighter than 4 mJy where the survey becomes 50 per cent complete at least in the regions with lower noise. There are only four sources brighter than 15 mJy and thus the number counts above 15 mJy are not included in Table 3.

Figure 8 shows that the 850-μm number counts in the NEP region are in good agreement with results from previous SCUBA-2 observations of other large cosmological fields (e.g., the 2.6 deg^2 of S2COSMOS, Simpson et al. 2019 or the 5 deg^2 of S2CLS, Geach et al. 2017) over the flux density range S_{850} = 4–15 mJy. Previous surveys showed that the 850-μm number counts are well described by a Schechter function. The dotted line in Fig. 8 is the best-fit Schechter function presented by Geach et al. (2017), which was the flux distribution of sources used for constructing artificial source catalogues use in the source recovery simulations (Section 3.1).

Although SMGs are usually selected in low-resolution,

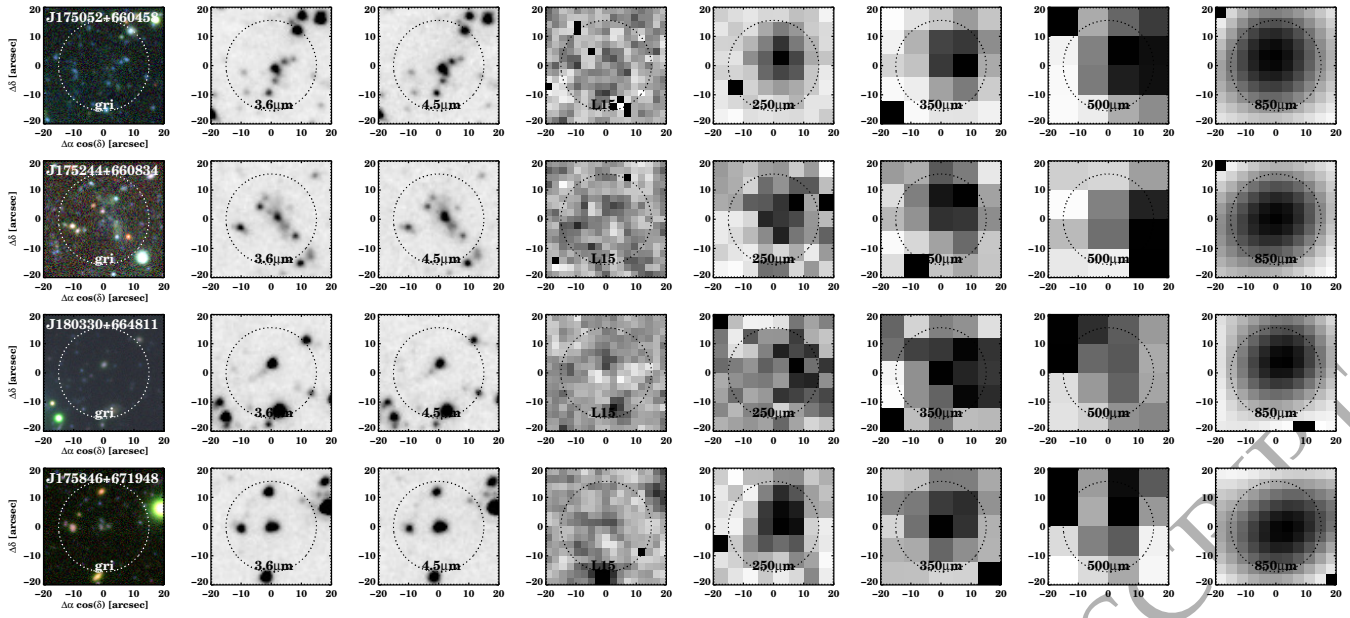

Figure 9. Cut-out images of the four brightest 850-μm sources, in order of appearance in the source catalogue (Table 2). All images have a size of 40 arcsec × 40 arcsec. The centre of each image, $(\Delta\alpha\cos\delta, \Delta\delta) = (0, 0)$, indicates the position of the 850-μm source. From left to right, we show: an optical colour composite image (Subaru/HSC g, r, i for blue, green and red, respectively); the *Spitzer*/IRAC 3.6- and 4.5-μm image; the *AKARI*/IRC 15-μm (L15) image; the *Herschel*/SPIRE 250-, 350- and 500-μm image; and the SCUBA-2 850-μm image. The dotted lines is a circle with 15 arcsec radius, i.e., the FWHM of the 850 μm beam. The top two sources (NEPSC_J175052+660458 and NEPSC2_J175244+660834) are associated with multiple objects at shorter wavelengths, the central object of which is very faint in the optical image. The source NEPSC2_J180330+664811 is relatively compact, and shows a faint tidal tail-like feature in the 3.6 and 4.5 μm images. The last source, NEPSC2_J175846+671948 is not spatially resolved at the resolution of IRAC, but in the HSC images the source breaks into three objects with similar colours.

wide-area single-dish surveys, recent follow-up observations using submm/mm interferometer arrays have suggested that individual single-dish submm sources often break up into multiple objects in a higher-resolution image (e.g., Karim et al. 2013; Hill et al. 2018; Stach et al. 2018; Simpson et al. 2020). The multiplicity is due to a mixture of physically associated galaxies and unrelated galaxies seen along the line of sight (Hayward et al. 2013). Therefore the number counts in single-dish surveys will tend to be affected by the effects of multiplicity. One of the early results using ALMA (Karim et al. 2013) reported that the number counts of bright submm sources above S_{850} = 9 mJy had been substantially overestimated based on the 1.5 arcsec resolution imaging of 122 SMGs selected in the 19 arcsec resolution Large Apex BOlometric CAmera (LABOCA) image. From the interferometric follow-up observations of the bright submm sources in the S2CLS UKIDSS/UDS field (AS2UDS; Stach et al. 2018, with Simpson et al. 2015 as a pilot study), it has been suggested that the normalization of the number counts above 5 mJy is 28 per cent lower than that of the SCUBA-2 counts, while the shape of the counts remains unchanged. The multiplicity rate is expected to increase as the flux density of sources increase (Stach et al. 2018), although the effect is found to be true only for the most luminous (> 12 mJy) sources (AS2COSMOS; Simpson et al. 2020). In addition, there is debate over the strength of the effect because it depends on the precise definition of 'multiplicity', in terms of the separation and flux density ratios of individual peaks within each source complex (see, e.g., Hill et al. 2018).

In Fig. 8, we also plot the number counts from interferometric observations, in order to estimate the possible multiplicity effect of the NEP source counts over the investigated flux range. To compare counts obtained at different submm wavelengths, we applied a ν^2 scaling: i.e., ALMA 870-μm number counts are assumed to be measured at 0.95× the SCUBA-2 850-μm flux density bin and SMA 860-μm counts are assumed to be measured at 0.98× the SCUBA-2 flux density bin. For sources above 10 mJy in the NEPSC2 survey, the effect of multiplicity needs to be investigated through future spatially-resolved sub/millimetre observations, since the number counts from different surveys begin to deviate in this flux density range.

As well as the possibility of multiple objects contributing to a single submm source, the number counts in the brightest flux-density bins are known to often be dominated by strongly lensed galaxies (Negrello et al. 2010; Vieira et al. 2010), even if low-redshift ($z < 0.1$) and Galactic sources are removed. The number density of lensed submm galaxies is relatively low if the lens candidate selection is based on a high flux density cut (e.g., S_{500} > 100 mJy in Wardlow et al. 2013, with a surface density of $0.14 \pm 0.04\,\mathrm{deg}^{-2}$), based on evidence from shallow surveys over 70–100 deg^2 (Vieira et al. 2010; Wardlow et al. 2013). However, Bourne et al. (2014) have suggested that lensed sources can contaminate number counts at even lower flux densities, i.e., less than 20–30 mJy in the 250–350 μm bands, suggesting that the weak lensing of *Herschel*/SPIRE sources by foreground structures are quite common. On the other hand, in S2COSMOS (Simpson et al. 2019), there has

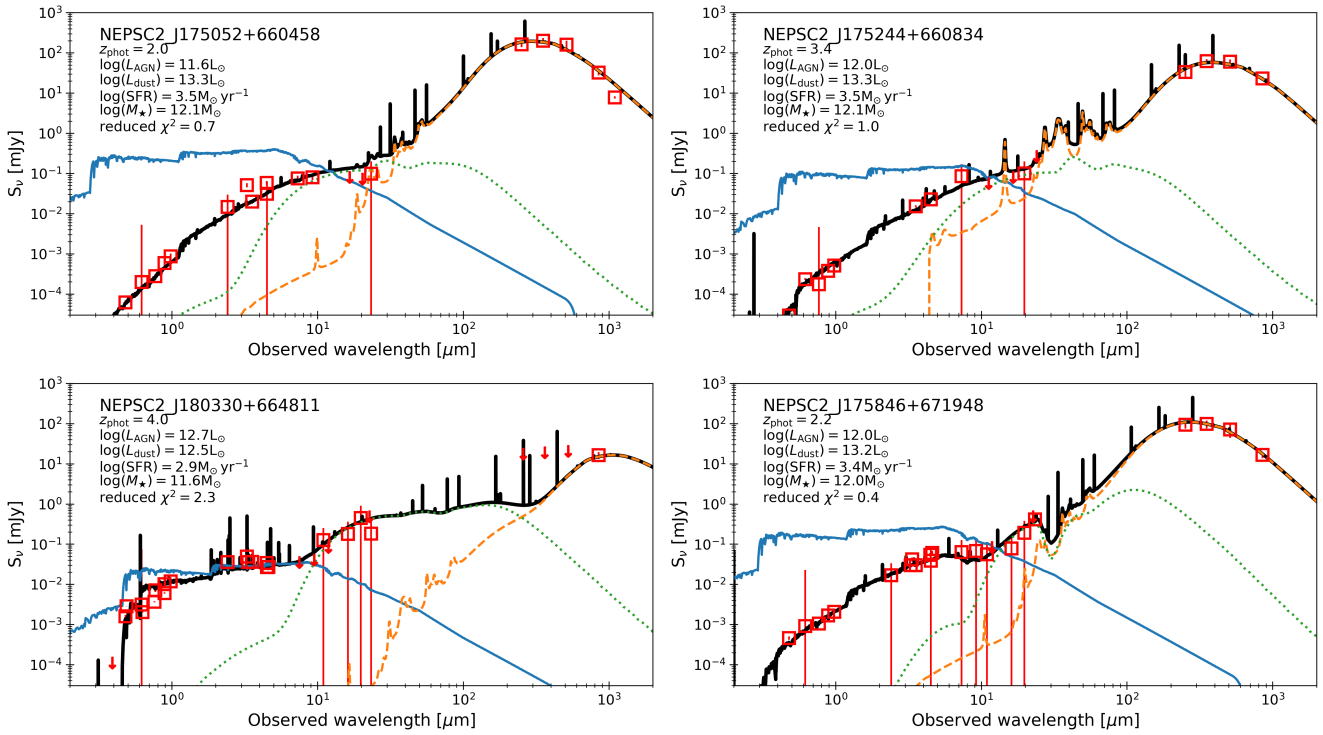

Figure 10. SEDs of the four brightest 850-μm sources ($S_{850} > 15$ mJy) from optical to submm wavelengths. Squares represent the observed flux densities from Subaru/HSC *grizy*, CFHT/megacam *ugriz*, *Spitzer*/IRAC 3.6 and 4.5 μm, *AKARI*/IRC 2–24 μm, *WISE* 3–22 μm, *Herschel*/SPIRE 250, 350, and 500 μm and SCUBA-2 850 μm (if available). The IRAM/NOEMA 1.3-mm data point is also overplotted for NEPSC_175052+660458. For photometric data lting below the 5σ detection level (i.e., detections between 3σ and 5σ), we assigned flux density uncertainties to be the same as the flux densities, hence the error bar appears to be larger compared to data points in other filters. Downward arrows indicate upper limits in the given filters, which corresponds to the 3 σ detection limit. Overplotted lines represent the best-fitting models, showing the results of CIGALE fitting; green dotted lines for the AGN component; orange dashed lines for the star-forming dust component; blue solid lines for the (unattenuated) stellar continuum component; and black solid lines for the sum of all the components.

been no evidence of such an excess at the bright end from the SCUBA-2 850-μm observations with beam size smaller than that of *Herschel*. The absence of such an excess in S2COSMOS is still statistically consistent with the results from S2CLS (Geach et al. 2017). In the NEP region, covering approximately 2 deg^2, four sources are found with S_{850} brighter than 15 mJy and two among those are brighter than 20 mJy. This is again statistically similar to the results of S2CLS/S2COSMOS; nevertheless it produces an enhancement in the number counts compared to the Schechter fit (orange circles in Fig. 8). To elucidate the nature of these brightest 850-μm sources, we present their images and SEDs in the following section.

4.2 Counterpart identification of 850-μm sources

While the full multi-wavelength identification of 850-μm sources and their characterisation will follow in another paper, here we briefly describe the way to find counterparts of submm sources in other wavelength data in order to determine the properties of four of the brightest sources with $S_{850} > 15$ mJy (as described in Section 4.3). Identification of the submm galaxies selected in wide-area surveys is not straightforward, especially when the source extraction procedure is not done using prior positions (Jin et al. 2018) because of the large beam size of single-dish observations. A frequently adopted approach is to use higher-resolution radio and/or mid-IR images (e.g., Chen et al. 2016; Michałowski et al. 2017; Cowie et al. 2018). For example, Lim et al. (2020) and Chang et al. (2018) used VLA 3-GHz source positions to find counterparts of 450-μm-selected sources, and relied on the 24-μm position if the 3-GHz position was not available. A machine-learning method combined with the radio data has been reported to be highly efficient for identifying multi-wavelength counterparts of submm galaxies (An et al. 2018, 2019). When high spatial resolution radio/mid-IR images are not available, an alternative way is to find a counterpart based on the likelihood-ratio method (Sutherland & Saunders 1992) using magnitudes or colours as variables. This approach has been widely applied to far-IR/submm surveys (e.g., Hwang et al. 2010; Chapin et al. 2011; Fleuren et al. 2012; Kim et al. 2012). From the fact that submm/mm galaxies tend to have red optical/near-IR colours compared to other (i.e., submm-faint) objects, a likelihood analysis using such colours is expected to identify 60–80 per cent of SCUBA-2 SMG counterparts (e.g., Pope et al. 2005; Michałowski et al. 2012; Alberts et al. 2013; Chen et al. 2016), although the actual identification rate varies along with details in the methodology selected by different authors.

The ancillary radio-imaging data in the NEP region are limited both in terms of the survey area and the sensitivity required to cross-identify 850-μm selected dusty sources that are not dominated by non-thermal radiation. The 1.5-GHz VLA imaging with $\sigma = 6\,\mu$Jy is available for 0.4 deg^2, but the coverage is limited to the central area inside which around 200 submm sources are located. Note that all four of the brightest sources presented here are located outside the VLA coverage. The spatial resolution of the available mid-IR imaging data (covering 2–24 μm) by the *AKARI*/IRC instrument (Onaka et al. 2007) is relatively poor, since the FWHM of the PSF is as large as 6 arcsec. *Spitzer*/MIPS 24-μm imaging data are available for central 1 deg^2, yet the sensitivity is also limited. Therefore we decided to mainly rely on the publicly available *Spitzer*/IRAC 3.6- and 4.5-μm imaging data (Nayyeri et al. 2018, PSF size approximately 1 arcsec) for the SMG counterpart identification. The [3.6−4.5] colour is used to construct a parameter distribution for SMGs. The counterparts of *Herschel*/SPIRE 250-, 350-, and 500-μm sources (Pearson et al. 2012) are also searched based on the [3.6 − 4.5] colours. If the SPIRE sources are located within one SCUBA-2 beam size from the positions of the SMGs, and if the IRAC counterpart of an SMG and that of a 250-μm-selected source (the SPIRE channel with the smallest beam size) are the same, we consider that the far-IR-to-submm (250–850 μm) emission is due to that single IRAC object. At shorter wavelengths, we use the Subaru/HSC *grizy* combined source catalogue over the NEP-Wide field (Oi et al. 2020, submitted) to find the nearest optical source from the position of an IRAC counterpart within the HSC PSF size (i.e., 0.8 arcsec). Among the 548 sources detected at 850 μm (excluding NGC 6543), IRAC counterparts are identified for 267 sources (about 50 per cent), with an estimated incorrect-counterpart rate for individual sources (based on *p*-values; Downes et al. 1986; Casey et al. 2013) of less than 5 per cent.

4.3 Properties of the brightest sources

As mentioned in Section 4.1, we found four 850-μm sources that are brighter than 15 mJy. This is slightly more than expected from the 2 deg^2 survey, i.e., two sources, if the source number density distribution follows the Schechter function. All four of these sources are located outside the S2CLS coverage. In the full S2CLS catalogue, over 5 deg^2 (Geach et al. 2017), there are five SMGs reported with $S_{850} > 15$ mJy: one in the NEP; one in the COSMOS; one in the EGS field; and the other two in the UDS field. The one in the NEP region is no longer in our updated mosaic map (see Section 3.3). The SMG in the COSMOS field is suggested to be a starburst at $z = 4.6$ from the optical spectroscopy (AzTEC/COSMOS 1, Smolčić et al. 2011). For the two SMGs in the UDS field, one is a luminous submm galaxy with the possibility of being optically dark and lensed by a foreground galaxy sharing the same line of sight (Orochi, Ikarashi et al. 2011). The other SMG comprises two counterparts in ALMA follow up (Dudzevičiūtė et al. 2020), with $z \sim 3.3$. In the S2COSMOS catalogue (Simpson et al. 2019), there are three SMGs with deboosted flux density larger than 15 mJy; the brightest components in ALMA follow up for these three SMGs are at $z = 3.4$, 4.3 and 2.7 (Simpson et al. 2020). All of the bright SMGs with $S_{850} > 15$ mJy are known to be located at redshifts that are higher than the median ($\langle z \rangle \simeq 2$) for 850-$\mu$m-selected SMGs. There is tentative evidence for a mild increase of redshift as a function of submm flux density (Ivison et al. 2002), and this trend is present even for the spatially resolved submm sources (Simpson et al. 2020). The four brightest SMGs found in the NEP field may be SMGs at high redshift whose number density is relatively low (if they do not suffer from the effects of source blending). In order to characterise these sources, we present multi-wavelength cut-out images in Fig. 9 and SEDs in Fig. 10.

Only one of these four sources, namely NEPSC2_J180330+664811, is isolated, showing a relatively compact morphology at optical-to-near-IR wavelengths, while the others appear to be associated with multiple galaxies seen in the optical/near-IR. For example, NEPSC2_J175846+671948 has at least three possible counterparts in the optical that are not resolved in the 3.6- and 4.5-μm image. For the other two sources (NEPSC2_J175052+660458 and NEPSC2_J175244+660834), the resolved galaxies are aligned along a filamentary-like structure, with diffuse, low surface-brightness emission around the galaxies. The aligned structure does not seem consistent with the arc-like features typically seen in gravitational lenses. Such an alignment of galaxies suggests the possibility of the bright 850-μm flux density being contributed by several star-forming galaxies that are physically associated, i.e., mergers. While more work (including interferometric follow-up observations) are needed in order to determine whether these multiple counterparts are physically associated or merely aligned by chance, the fact that most of the bright sources appear to be multiples is consistent with the previous findings. For example, two of the luminous 850-μm sources above 15 mJy in the aforementioned S2CLS-UDS field turned out to be composed of two components in ALMA images (Stach et al. 2019). The brightest source in the NEPSC2 catalogue, NEPSC2_J175052+660458, was observed by the IRAM NOrthern Extended Millimetre Array (NOEMA) being selected as a candidate lensed galaxy based on the *Herschel*/SPIRE photometry (Burgarella et al. 2019). In the 1.3-mm continuum image, the source (designated as 'NEP-12' in Burgarella et al. 2019) is resolved into three components. Broadly speaking, the optical and/or radio interferometer images of NEPSC2 bright sources support the idea that the multiplicity rate is higher than or comparable to 50 per cent at flux limits brighter than 15 mJy (Stach et al. 2018; Simpson et al. 2020).

The SEDs of the four bright NEP sources are constructed using the multi-wavelength identification procedure described in Section 4.2. Optical *grizy* magnitudes of NEPSC2_J175052+660458, NEPSC2_J175244+660834 and NEPSC2_J175846+671948 are taken from the optical source closest to the position measured at 4.5 μm. SED fitting is carried out using CIGALE[2] (Code Investigating GAlaxy Emission: Noll et al. 2009; Boquien et al. 2019). CIGALE computes the spectral models based on an energy balance principle between the UV (mainly from direct stellar radiation) and the IR (mainly from dust-reprocessed stellar radiation), enabling one to efficiently estimate the physical properties of

[2] https://cigale.lam.fr/2018/11/07/version-2018-0/

galaxies such as SFRs, attenuation, dust luminosities, stellar masses and the contributions from an AGN, by fitting the observed data to a grid of several million models. It is also possible to derive the photometric redshifts of galaxies if a grid of photometric redshifts are provided. Since we do not have spectroscopic redshifts for the four bright 850-μm sources, we run CIGALE in a photometric redshift mode (sampling z = 0.1–5, with a redshift step of Δz = 0.1) to find the possible redshift and the best-fitting SED model simultaneously.

We used a delayed star-formation history model that is flexible enough to fit the high-SFR galaxies in the early Universe (Ciesla et al. 2017), by fixing the e-folding time, but varying the age of the main stellar population. For a single stellar population, the *bc03* (i.e., Bruzual & Charlot 2003) library with solar metallicity and Salpeter (1955) initial mass function was chosen, with the addition of a treatment of nebular emission. To model the dust attenuation and the dust emission, we chose to use the Charlot & Fall (2000) method with a range of A_V, and the Draine et al. (2014) model with a range of PAH mass fraction that has also been applied to fit the SEDs for mid-IR-selected *AKARI* galaxies (Toba et al. 2020; Wang et al. 2020, submitted). In fitting the warm dust component from an AGN contribution that dominates the mid-IR, we parameterised the optical depth at 9.7 μm, the opening angle, the angle between the equatorial axis and the line of sight, and the AGN fraction, all based on the study described in Fritz, Franceschini, and Hatziminaoglou (2006).

All four of the sources are expected to be at $z > 2$, with the photometric redshift ranging over $z_{\rm phot}$ = 2.4–4.0. The total IR luminosities range over 0.8–2.1$\times10^{13}$ L$_\odot$, as expected from the the clear far-IR/submm detection at a level of a few tens of mJy. Three of the four sources are dominated by star-formation, with a minor AGN contribution ranging between 2 and 5 per cent. For only one of the sources, NEPSC2_J180330+664811, does the AGN dominate (with an AGN contribution of 60 per cent). This is in agreement with the expectation from the multi-wavelength cut-out images, i.e., the SED of the relatively isolated, compact source (NEPSC2_J180330+664811) shows a high fraction of AGN contribution, while the SEDs of others are close to that of dusty star-forming galaxies with A_V = 3–4 mag. While the three sources with star-formation-dominated SEDs are detected in *Herschel*/SPIRE 250, 350 and 500 μm imaging, NEPSC2_J180330+664811 is not detected in any of the *Herschel*/SPIRE channels. If this source truly lies at $z \gtrsim 4$, as would be expected from its non-detection in the u-band and at 250–500 μm, this example shows that the 850-μm data provide a powerful tool to select $z > 4$ bright, obscured AGN that are missed by *Herschel*/SPIRE. Unfortunately, the X-ray areal coverage (Krumpe et al. 2015; Miyaji et al. 2017) is limited to only the central 0.4 deg^2, therefore the confirmation of this source being an obscured AGN requires further follow-up observations.

Note that the parameters derived through the SED fitting, including far-IR luminosities, reddening, and photometric redshifts are affected by the fact that multiple sources could contribute in the 850-μm emission. For example, in case of the source NEPSC_J175052+660458, Burgarella et al. (2019) showed that each component of the source fitted to have photometric redshifts at z = 1.83 and 1.98, while using the integrated flux density points to the photometric redshift of z = 2.17. The photometric redshift can be elevated due to the source multiplicity, therefore careful counterpart identification based on the multi-wavelength imaging and spatially resolved sub/millimetre observations is needed to correctly constrain redshift and nature of bright submm sources. With the interferometric follow up observations, the submm fluxes included in the SED fitting may need to be corrected for contributions from any confused companions.

5 CONCLUSIONS

We have presented an 850-μm mosaiced map and source catalogue for the NEP region, using archival data and around 200 hours of new data from the EAO/JCMT large programme NEPSC2 taken up until 2019. The total area covered by the final map is approximately 2 deg^2 if we limit ourselves to the area with rms instrumental noise better than 2.7 mJy beam^{-1}. This area is more than 3 times larger than the previous 850-μm coverage of the NEP. In the deepest region, the rms noise of the combined map reaches 1.0 mJy beam^{-1}, i.e., close to the 850-μm confusion limit. Adopting a detection threshold at 4σ, we extract 549 submm sources, of which we estimate 10 per cent to be false detections (i.e., either not a genuine source or else a source that is substantially fainter and boosted by noise). The false-detection rate becomes less than 3 per cent if we adopt a 4.5σ detection threshold, while the number of 850-μm sources becomes 342. The 50 per cent source completeness limit occurs at flux densities between 3.9 and 8.5 mJy, depending on the source locations within the map. As part of this publication, we are releasing the 850-μm mosaic map and catalogue.

Our number counts of 850-μm sources detected in the NEP show good agreement with those from other extragalactic cosmological blank fields (Geach et al. 2017; Simpson et al. 2019) and are well described by a Schechter function. This means that our 2 deg^2 area around the NEP is neither especially overpopulated or underpopulated, which is what we expect because degree-scale fields are wide enough that the excess variance due to clustering should be small. The mild excess at the bright end is contributed by a few $S_{850} > 15$ mJy sources. There are possibilities that such bright sources are either high-redshift AGN or groups of star-forming galaxies that are not resolved in the single-dish FIR/submm observations; these possibilities can be distinguished using interferometric follow up observations.

An extension of the NEPSC2 to complete the 850-μm mapping over the entire 4 deg^2 has recently been approved (JCMT program ID M20AL005). Based on the number of new 850-μm sources outside the S2CLS coverage, we expect to detect about 400 new sources once the extension has been completed. The number of rare, bright SMGs should be doubled, opening the possibility of studying galaxy cluster-scale structures at different redshifts, as well as discovering 850-μm-bright obscured AGN at $z > 4$ that have been missed in the *Herschel*/SPIRE observations.

6 DATA AVAILABILITY

The data underlying this article are available in Zenodo, at https://dx.doi.org/10.5281/zenodo.3897405.

ACKNOWLEDGEMENTS

The James Clerk Maxwell Telescope is operated by the East Asian Observatory on behalf of: The National Astronomical Observatory of Japan; Academia Sinica Institute of Astronomy and Astrophysics; the Korean Astronomy and Space Science Institute; and the Center for Astronomical Mega-Science (as well as the National Key R&D Program of China with No. 2017YFA0402700). Additional funding support is provided by the Science and Technology Facilities Council of the United Kingdom and participating universities in the United Kingdom and Canada. Additional funds for the construction of SCUBA-2 were provided by the Canada Foundation for Innovation. The data presented in this paper were taken as part of Program ID M17BL007, and archival data from Program ID MJLSC02 were used to produce the combined map. H. Shim, Y. Kim and D. Lee acknowledge support from the National Research Foundation of Korea (NRF) grant, No. 2018R1C1B6008498, funded by the government of Korea (MSIT). TH is supported by the Centre for Informatics and Computation in Astronomy (CICA) at National Tsing Hua University (NTHU) through a grant from the Ministry of Education of the Republic of China (Taiwan). MI acknowledges support from the National Research Foundation of Korea grant, No. 2020R1A2C3011092. MPK acknowledges support from the First TEAM grant of the Foundation for Polish Science No. POIR.04.04.00-00-5D21/18- 00. MJM acknowledges the support of the National Science Centre, Poland, through the SONATA BIS grant 2018/30/E/ST9/00208. The Cosmic Dawn Center is funded by the Danish National Research Foundation.

REFERENCES

Alberts S. et al., 2013, MNRAS, 431, 194
An F.X. et al., 2018, ApJ, 862, 101
An F.X. et al., 2019, ApJ, 886, 48
Banerji M. et al., 2015, MNRAS, 454, 419
Barger A.J. et al., 2014, ApJ, 784, 9
Blain A.W., Smail I., Ivison R. J., Kneib J.-P., Frayer, D.T., 2002, Physics Report, 369, 111
Bourne N. et al. 2014, MNRAS, 444, 1884
Boquien M., Burgarella D., Roehlly Y., Buat V., Ciesla L., Corre D., Inoue A. K., Salas H., 2019, A&A, 622, 103
Brisbin D. et al., 2017, A&A, 608, 15
Bruzual G., Charlot S., 2003, MNRAS, 344, 1000
Burgarella D. et al., 2019, PASJ, 71, 12
Casey C.M. et al., 2013, MNRAS, 436, 1919
Casey C.M., Narayanan D., Cooray A., 2014, Physics Reports, 541, 45
Cavanagh B., Jenness T., Economou F., Currie M. J., 2008, The ORAC-DR data reduction pipeline, Astron. Nactr., 329, 295 (DOI:10.1002/asna.200710944)
Chang Y.-Y. et al., 2018, ApJ, 865, 103
Chapin E.L., Chapman S.C., Coppin K.E., Devlin M.J., Dunlop J.S. et al., 2011, MNRAS, 411, 505
Chapin E.L., Berry D.S., Gibb A.G., Jenness T., Scott D., Tilanus R.P., Economou F., Holland W.S., 2013, MNRAS, 430, 2545
Chapman S.C., Windhorst R., Odewahn S., Yan H., Conselice C., 2003, ApJ, 599, 92
Chapman S.C., Blain A.W., Smail I., Ivison R.J., 2005, ApJ, 622, 772
Charlot S., Fall S.M., 2000, ApJ, 539, 718
Chen C.-C. et al., 2016, ApJ, 820, 82
Ciesla L., Elbaz D., Fensch, J., 2017, A&A, 608, 41
Cooray A. R., 2019, Nature Astronomy, 3, 885
Coppin K., Halpern M., Scott D., Borys C., Chapman S., 2005, MNRAS, 357, 1022
Coppin K., Chapin E.L., Mortier A,M.J., Scott S.E., Borys C. et al., 2006, MNRAS, 372, 1621
Cowie L.L., Gonzalez-Lopez J., Barger A.J., Bauer F.E., Hsu L.-Y., Wang, W.-H., 2018, ApJ, 865, 106
Dannerbauer H. et al., 2014, A&A, 570, 55
Dempsey J. T. et al., 2013, MNRAS, 430, 2534
Downes A.J.B., Peacock J.A., Savage A., Carrie D.R., 1986, MNRAS, 218, 31
Draine B.T. et al., 2014, ApJ, 780, 172
Dudzevičiūtė U. et al., 2020, MNRAS, 494, 3828
Eddington A.S., 1913, MNRAS, 73, 359
Fleuren S. et al., 2012, MNRAS, 423, 2407
Fritz J., Franceschini A., Hatziminaoglou E., 2006, MNRAS, 366, 767
Geach J.E., Smail I., Chapman S.C., Alexander D.M., Blain A.W., Stott J.P., Ivison R.J., 2007, ApJL, 655
Geach J.E. et al., 2017, MNRAS, 465, 1789
Gonzalez J.E., Lacey C.G., Baugh C.M., Frenk, C.S., 2011, MNRAS, 413, 749
Greve T.R. et al., 2005, MNRAS, 359, 1165
Hainline L.J., 2008, PhD thesis, California Institute of Technology
Hayward C.C. et al., 2013, MNRAS, 434, 2572
Hill R. et al., 2018, MNRAS, 477, 2042
Hodge J.A. et al., 2013, ApJ, 768, 91
Holland W.S. et al., 2013, MNRAS, 430, 2513
Hwang N. et al., 2007, ApJS, 172, 583
Hwang H.S. et al., 2010, MNRAS, 409, 75
Hwang H.S., Elbaz D., Lee J.C., Jeong W.-S., Park C., Lee M.G., Lee H.M., 2010, A&A, 522, 33
Ikarashi S. et al., 2011, MNRAS, 415, 3081
Ivison R.J. et al., 2002, MNRAS, 337, 1
Ivison R.J. et al., 2007, MNRAS, 380, 199
Jin S. et al., 2018, ApJ, 864, 56
Karim A. et al., 2013, MNRAS, 432, 2
Kim S.J. et al., 2012, A&A, 548, 29
Kim S. et al., 2012, ApJ, 756, 28
Komatsu E. et al., 2011, ApJS, 192, 18
Koprowski M.P. et al., 2016, MNRAS, 458, 4321
Krumpe M. et al. 2015, MNRAS, 446, 91Krumpe M. et al. 2015, MNRAS, 446, 9111
Laureijs R. et al. 2011, *Euclid Definition Study Report (Red Book)*, arXiv:1110.3193
Le Floc'h E. et al., 2005, ApJ, 632, 169
Lim C.-F. et al., 2020, ApJ, 889, 80
Liu D. et al., 2019, ApJS, 244, 40
Magnelli B. et al., 2013, A&A, 553, 132
Matsuhara H. et al., 2006, PASJ, 58, 673
Menendez-Delmestre K., Blain A. W., Swinbank M., Smail I., Ivison R. J., Chapman S. C., Goncalves, T. S., 2013, ApJ, 767, 151
Michałowski M., Hjorth J., Watson D., 2010, A&A, 514, 67
Michałowski M. J. et al., 2012, MNRAS, 426, 1845
Michałowski M.J., Hayward C.C., Dunlop J.S., Bruce V.A., Cirasuolo M., Cullen F., Hernquiest L., 2014, A&A, 571, 75
Michałowski M.J. et al., 2017, MNRAS, 469, 492
Miller T. B., Hayward C. C., Chapman S. C., Behroozi P. S., 2015, MNRAS, 452, 878
Miyaji T. et al., 2017, PKAS, 32, 235

Nayyeri H. et al., 2018, ApJS, 234, 38
Negrello M. et al., 2010, Science, 330, 800
Noll S., Burgarella D., Giovanni E., Buat V., Marcillac D., Munoz-Mateos J. C., 2009, A&A, 507, 1793
Oi N. et al., 2014, A&A, 566, 60
Onaka T. et al., 2007, PASJ, 59, 401
Pearson C. et al., 2012, PKAS, 27, 375
Planck Collaboration, 2020, A&A, in press, arXiv:1807.06209
Pope A., Borys C., Scott D., Conselice C., Dickinson M., Mobasher B., 2005, MNRAS, 358, 149
Riechers D.A. et al., 2010, ApJL, 720, 131
Salpeter E.E., 1955, ApJ, 121, 161
Simpson J.M. et al., 2014, ApJ, 788, 125
Simpson J.M. et al., 2015, ApJ, 807, 128
Simpson J.M. et al., 2017, ApJ, 839, 58
Simpson J.M. et al., 2019, ApJ, 880, 43
Simpson J.M. et al., 2020, MNRAS, 495, 3409
Smail I., Ivison R. J., Blain A.W., Kneib, J.-P., 1998, ApJL, 507, 21
Smolčić V. et al., 2011, ApJL, 731, 27
Smolčić V. et al., 2012, A&A, 548, 4
Smolčić V. et al., 2015, A&A, 576, 127
Smolčić V. et al., 2017, A&A, 597, 4
Stach S.M. et al., 2018, ApJ, 860, 161
Stach S.M. et al., 2019, MNRAS, 487, 4648
Sutherland W., Saunders W., 1992, MNRAS, 259, 413
Tacconi L.J. et al., 2006, ApJ, 640, 228
Takagi T. et al., 2012, A&A, 537, 24
Thomas H.S., Currie M. J., 2014, Starlink Cookbook 21
Toba Y., Ueda J., Lim C.-F., Wang W.-H., Nagao T., Chang Y.-Y., Saito T., Kawabe R., 2018, ApJ, 857, 31
Toba Y. et al., 2020, ApJ, 889, 76
Toba Y. et al., 2020, ApJ, 899, 35
Toft S. et al., 2014, ApJ, 782, 68
Ueda Y. et al., 2018, ApJ, 853, 24
Vieira J.D. et al., 2010, ApJ, 719, 763
Wang S. X. et al., 2013, ApJ, 778, 179
Wardlow J.L. et al., 2013, ApJ, 762, 59
Whitaker K.E., Pope A., Cybulski R., Casey C.M., Popping G., Yun M.S., 2017, ApJ, 850, 208
White G.J. et al., 2010, A&A, 517, 54